JACS
JOURNAL OF THE AMERICAN CHEMICAL SOCIETY

ARTICLE

pubs.acs.org/JACS

Heterogeneous Binding of Dioxygen: EPR and DFT Evidence for Side-On Nickel(II)−Superoxo Adduct with Unprecedented Magnetic Structure Hosted in MFI Zeolite

Piotr Pietrzyk,* Katarzyna Podolska, Tomasz Mazur, and Zbigniew Sojka

Faculty of Chemistry, Jagiellonian University, ul. Ingardena 3, 30-060 Krakow, Poland

Supporting Information

ABSTRACT: This article reports on the activation of dioxygen on nickel(I) dispersed inside the nanopores of the ZSM-5 zeolite, which can be regarded as a heterogeneous mimetic system (zeozyme) for Ni-bearing enzymes. The side-on η^2-coordination of the resulting nickel-bound superoxo adduct was ascertained by detailed analysis of the EPR spectra of both $^{16}O_2$ and $^{17}O_2$ species supported by computer simulations of the spectra and relativistic DFT calculations of the EPR signatures. Molecular analysis of the $\boldsymbol{g}$ and $\boldsymbol{A}(^{17}O)$ tensors (g_{xx} = 2.0635, g_{yy} = 2.0884, g_{zz} = 2.1675; $|A_{xx}| \approx 1.0$ mT, $|A_{yy}|$ = 5.67 mT, $|A_{zz}| \approx 1.3$ mT) and quantum chemical modeling revealed an unusual electronic and magnetic structure of the observed adduct (with $g_{zz}(g_{max}) > g_{yy}(g_{mid}) > g_{xx}(g_{min})$ and the largest O-17 hyperfine splitting along the g_{mid} direction) in comparison to the known homogeneous and enzymatic nickel−superoxo systems. It is best described as a mixed metalloradical with two supporting oxygen donor ligands and even triangular spin-density redistribution within the η^2-$\{NiO_2\}^{11}$ magnetophore. The semioccupied molecular orbital (SOMO) is constituted by highly covalent δ overlap between the out-of-plane $2p(\pi_g^*)$ MO of dioxygen and the $3d_{x^2-y^2}$ MO of nickel. By means of the extended transition state-natural orbitals for the chemical valence approach (ETS-NOCV), three distinct orbital channels (associated with σ, π, and δ overlap) of congruent and incongruent charge and spin density flows within the η^2-$\{NiO_2\}^{11}$ unit, contributing jointly to activation of the attached dioxygen, were identified. Their individual energetic relevance was quantified, which allowed for explaining the oxygen binding mechanism with unprecedented accuracy. The nature and structure sensitivity of the $\boldsymbol{g}$ tensor was rationalized in terms of the contributions due to the magnetic field-induced couplings of the relevant molecular orbitals that control the $\boldsymbol{g}$-tensor anisotropy. The calculated O-17 hyperfine coupling constants correspond well with the experimental parameters, supporting assignment of the adduct. To the best of our knowledge, the η^2-$\{NiO_2\}^{11}$ superoxo adducts have not been observed yet for digonal mononuclear nickel(I) centers supported by oxygen donor ligands.

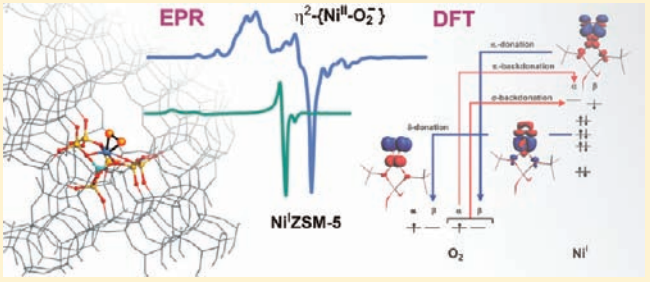

1. INTRODUCTION

Zeolites are crystalline aluminosilicates with a three-dimensional framework containing regular, well-defined void spaces of molecular dimensions.[1] Such three-dimensional structure provides cages (pockets) and channels able to accommodate guest molecules and is responsible for unique supramolecular steric and space confinement effects.[1−3] They not only may restrict the molecular traffic within the intrazeolitic channels but also can stabilize reactants, products, and transition states promoting desired catalytic reaction to proceed in the way resembling in many aspects the action of enzymes.[4] Paramount examples are provided by biomimetic reactions of metallozeolites containing various transition-metal ions, such as room-temperature oxidation of the C−H bond over FeZSM-5 catalysts, reminiscent of the methane monooxygenase,[5] or decomposition of N_2O over CuZSM-5,[6] analogous to the copper enzyme nitrous oxide reductase (N_2OR).[7] Furthermore, biologically relevant Ni carbonyl complexes can mimic the activity of acetylcoenzyme A (acetyl-CoA) synthases[8] or dihydrogen oxidation by hydrogenases.[9] Such remarkable functional similarity with the more complex enzymatic systems allows for considering zeolites as "solid enzymes", sometimes called by the generic name zeozymes.[4]

The low reactivity of the gas-phase dioxygen toward organic molecules is an inherent feature of its high-spin ground state ($^3\Sigma_g^-$). This spin barrier can be circumvented easily upon interaction with transition-metal ions. The variety of the shapes and favorable orientations of energetically accessible d orbitals together with the multiplicity of the valence and spin states allow transition-metal species to react with dioxygen without violating symmetry and spin conservation rules.[10,11] The first step in oxygen activation by a wide variety of metallozeolites and metalloenzymes is binding of the dioxygen molecule resulting in electron transfer from metal to ligand to form a metal−superoxo ($1e^-$ reduction) or −peroxo ($2e^-$ reduction) species. It may next be followed by O−O bond cleavage, leading to formation of

Received: September 5, 2011
Published: October 28, 2011

high-valent metal−oxo cores ($4e^-$ reduction). All forms of the activated oxygen species are believed to carry out oxidation of exogenous organic reactants.[12,13] In biomimetic coordination chemistry various mononuclear metal−O_2 complexes including manganese, iron, cobalt, and copper as well as many other first-, second-, and third-row transition metals have been synthesized, isolated, and characterized with a range of spectroscopic techniques and X-ray crystallography.[14−16] The mode of O_2 coordination (side-on vs end-on) and the electronic nature of the metal−O_2 core (superoxo vs peroxo) were found to vary depending on the metal center and the nature of the supporting ligands. It is additionally complicated by the subtle magnetic interactions, since many of the transition-metal ions exhibit high-spin ground states. In this context, the search for novel biomimetic systems and molecular environments for hosting metal cores capable of making O_2 more reactive toward hydrocarbon activation while avoiding autoxidation and overoxidation processes is still a challenging issue.

The paramagnetic mononuclear nickel−dioxygen $\{NiO_2\}^{11}$ adducts are the key species implicated in various important homo- and heterogeneous catalytic systems including enzymatic processes.[17−20] Both side-on (η^2) and end-on (η^1) nickel−superoxo and side-on (η^2) nickel−peroxo complexes have been synthesized and characterized by spectroscopic, X-ray crystallographic, and computational methods.[20−24] The nickel(II)−superoxo complexes were usually described as the O_2^- species coupled antiferromagnetically with high-spin Ni(II) to yield a $S = 1/2$ system with the $|d_{z^2}\rangle$ ground state configuration ($\uparrow Ni^{II}\downarrow\uparrow O_2^-$). The same $|d_{z^2}\rangle$ ground state has also been postulated for the Ni^{III}−peroxo formulation of the nickel−dioxgen adducts due to the low-spin $3d^7$ ($S = 1/2$) configuration ($\uparrow\downarrow\uparrow Ni^{III}-O_2^{2-}$), making the distinction of both species by electron paramagnetic resonance (EPR) spectroscopy difficult.[25]

To understand the fundamental chemistry of the $\{NiO_2\}^{11}$ unit for accurate control of its reactivity, a detailed atomic level description of the electronic and magnetic structure of this species in discrete and embedded states is of great cognitive value. Indeed, it has been shown recently that activation of dioxygen in model complexes mimicking metalloenzymes is controlled by the spin-dependent topology and polarization of the electron-pair density around the oxygen moiety.[26] In this context, establishment of the ground spin state of the $\{NiO_2\}^{11}$ unit is important for better understanding of its reactivity as it may severely influence the activation entropies.[10]

Among various spectroscopic techniques applied for such investigations, EPR spectroscopy has widely been used due to the paramagnetic nature of the $\{NiO_2\}^{11}$ species.[8] Yet, quantitative molecular interpretation of the corresponding EPR parameters ($\boldsymbol{g}$ and $\boldsymbol{A}(^{17}O)$ tensors) in terms of the electronic structure of the adduct is not a trivial task, taking into account an intricate nature of the magnetic interactions within the nickel−dioxygen unit and its nearest molecular environment as well as the constraints imposed by rather common low local symmetry.

Thanks to modern relativistic density functional theory (DFT) methods such as the zeroth-order regular approximation (ZORA)[27] or spin−orbit mean-field approximation (SOMF),[28] fairly accurate calculations of EPR parameters are becoming accessible even for large systems containing transition-metal ions. The molecular nature of the $\boldsymbol{g}$ tensor can be revealed further using the scalar Pauli Hamiltonian.[29] Theoretical predictions of the $\boldsymbol{g}$ tensor for nickel(I) complexes have focused so far mostly on biomimetic systems,[30,31] homogeneous complexes,[32] and paramagnetic adducts with CO[28] and NO[33] in zeolite environments. However, for extended nonmolecular systems it is not easy to construct an exact model for advanced in-depth analysis of the relevant EPR parameters. Yet, conceptually useful results can be achieved already by analyzing simpler models that can next be embedded into the broad range of conceivable chemical environments with pliant (complexes), semirigid (enzymes), and rigid (zeolite frameworks) ligands.

Herein, we report the results of spectroscopic continuous wave CW-EPR and computational DFT investigations that have led to the observation of a side-on nickel−dioxygen adduct with a unique magnetic structure giving rise to the reversed $\boldsymbol{g}$ tensor. To the best of our knowledge, the η^2-$\{NiO_2\}^{11}$ superoxo adducts have not been observed yet for digonal mononuclear nickel(I) centers supported by oxygen donor ligands. We provide a detailed theoretical account for the electronic and magnetic structure of the investigated adduct. In view of the variety of local environments within which the $\{NiO_2\}^{11}$ unit may reside, we investigated more closely the molecular nature of the $\boldsymbol{g}$ and ^{17}O hyperfine tensors in terms of the local symmetry and the coordination state (η^1, η^2, and μ) of the model dioxygen congeners. Additionally, as shown by us earlier,[34,35] using a range of simplified molecular species of strictly defined point symmetry, EPR characterization of the transition-metal adducts can be rationalized through detailed insight into the magnetic field-induced couplings between the relevant molecular orbitals that contribute to the experimentally observed $\boldsymbol{g}$-tensor anisotropy.[36]

2. EXPERIMENTAL AND COMPUTATIONAL DETAILS

2.1. Materials. Nickel-exchanged zeolites were obtained by a standard ion-exchange method using a parent ammonium form of the ZSM-5 zeolite (Zeolyst, Inc.) with the Si/Al ratio equal to 15 and 40. The final pH of the solution varied from 2 to 5. Chemical analysis by means of the AAS method revealed Ni/Al exchange degrees of 54% (1.10 Ni wt %) and 40% (0.41 Ni wt %). Because the spectroscopic results obtained for both samples were virtually the same, all spectra shown hereafter correspond to the NiZSM-5(Si/Al = 15) sample. After drying, prior to the spectroscopic measurements, the samples were activated in a vacuum of 10^{-5} mbar at 773 K for 2 h (with a heating rate of 6 K/min), reduced with CO (Aldrich, 99.95%) at 673 K for 30 min, and finally evacuated at 553 K. The superoxide radical anions were generated by exposure of the reduced samples to 1−2 Torr of the naturally abundant (Aldrich, 99.95%) or ^{17}O-enriched dioxygen (Icon Service Inc., New Jersey). In the latter case, relative abundances (P^{nn}) of the $^{16}O_2$, $^{17}O^{16}O$, and $^{17}O_2$ isotopomers present in the gas mixture are given by $P^{16-16} = (1-p)^2 = 20\%$, $P^{16-17} = 2p(1-p) = 49\%$, and $P^{17-17} = p^2 = 31\%$, where $p = 55.5\%$ is the ^{17}O-enrichment level.

2.2. Characterization. CW-EPR spectra were recorded at 77 K with a Bruker ELEXSYS-E580 X-band spectrometer using a rectangular TE_{102} cavity with 100 kHz field modulation. The microwave power of 1−100 mW and the modulation amplitude of 0.2−0.5 mT were applied. Spectra processing was performed with the software provided by Bruker, whereas for computer simulations of the spectra the EPRsim32 program,[37] which calculates exact solutions for the spin-Hamiltonian by full matrix diagonalization, was used. A hybrid search procedure combining the genetic algorithm and Powell refinement was applied for optimization of the simulated spectra.

2.3. DFT Modeling. Zeolite sites acting as rigid multidentate macroligands for hosting the nickel−dioxygen unit were modeled using geometrically embedded clusters of various numbers of **T** atoms (**T** = Si or Al). A robust $\{NiO_2\}^{11}[Si_6AlO_8(OH)_{12}]$ cluster, referred to as **M7**, and a smaller reference $\{NiO_2\}^{11}[Si_2AlO_4H_8]$ one (**I2** site) were

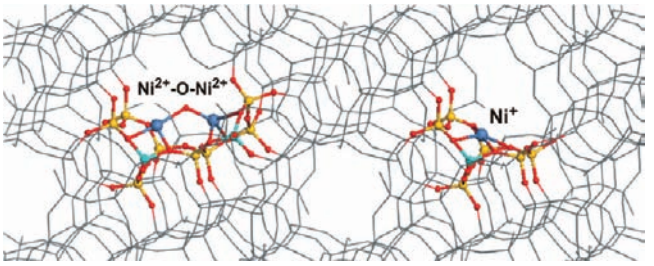

Figure 1. Localization of the cage dinuclear Ni(II)−O−Ni(II) and mononuclear Ni(I) sites within the channels of the ZSM-5 zeolite.

optimized within C_1 and C_s symmetry, respectively. In addition to the zeolite-embedded systems, four congener molecular complexes of the $\{NiO_2\}^{11}L_n$ type with the pliant aqua and hydroxyl ligands, $\{NiO_2\}^{11}(OH)$, $\{NiO_2\}^{11}[(H_2O)_2]$, $\{NiO_2\}^{11}[(OH)(H_2O)]$, and $\{NiO_2\}^{11}[(OH)(H_2O)_2]$, were used for modeling the influence of the coordination state on the calculated *g*-tensor values. In fact, it is well documented that the surface functional groups (≡Si(Al)OSi≡, ≡Si−OH) of the zeolitic support, which play the role of ligands constituting the first coordination sphere of the nickel center, are placed close to H_2O and OH^- ligands in the extended spectrochemical series.[38] The $\{NiO_2\}^{11}$ unit, both in bare and coordinated states, was fully optimized using analytical gradients, while the zeolite-embedded species (associated with the **M7** and **I2** sites) were optimized with geometrical constraints imposed on the terminal hydrogen atoms to account for the rigidity of the zeolite framework.

Relativistic DFT modeling was carried out for Ni^{I}ZSM-5 and $\{NiO_2\}^{11}$ZSM-5 complexes by means of the ADF program suite (version 2007.01)[39,40] at the spin-unrestricted level. The exchange-correlation potential of Becke88[41] and Perdew86[42] along with the scalar relativistic ZORA method were applied for geometry optimization. The all-electron basis set, denoted as TZP, was used for all atoms.[43] The structure of the cluster models was optimized with the analytic gradients and BFGS method, within the SCF electron density convergence criterion of 10^{-6} au, the gradient criterion of 3×10^{-3} au/Å, and the maximum displacement criterion of 3×10^{-3} Å. The natural orbitals for chemical valence (NOCV) combined with the Ziegler−Rauk extended transition state energy decomposition scheme (ETS-NOCV)[44,45] and the molecular diagram pictures using fragment molecular orbital (FMO) analysis were performed using the ADF program. Originally, ETS-NOCV analysis has been proposed for the closed-shell systems, allowing for separation and quantification of the electron charge transfer channels. In such a case the pairs of the natural orbitals for chemical valence (Ψ_{-k},Ψ_k) factorize the differential density $(\Delta\rho)$ into the particular NOCV contributions $(\Delta\rho_k)$[44]

$$\Delta\rho(r) = \sum_{k=1}^{M/2} \nu_k[-\psi_{-k}^2(r) + \psi_k^2(r)] \quad (1)$$

where ν_k and M stand for the NOCV eigenvalues and the number of basis function, respectively. For the open-shell systems the summation of the α and β electron densities should be carried out separately over the spin orbitals of virtually the same symmetry but not necessarily possessing the same ν_k values.

Single-point calculations of the *g* tensors involved double group symmetry adopted functions and spin−orbit coupling (SOC) included self-consistently to account for relativistic effects within the two-component, spin-unrestricted ZORA collinear method.[27,46] In addition, the one-component approach due to Schreckenbach and Ziegler[29] was applied for construction of the molecular diagrams of magnetic field-induced couplings. The *g* tensor was also calculated with the Neese method implemented in the ORCA software[47] within the mean-field approximation

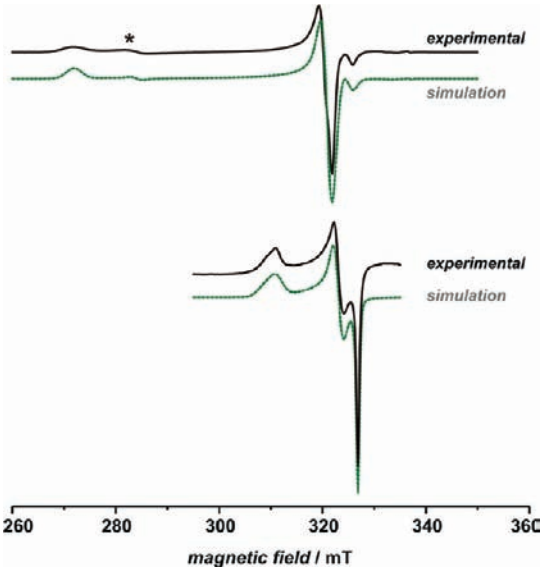

Figure 2. X-band CW-EPR of (a) parent Ni^{I}ZSM-5 sample and (b) $^{16}O_2$ adduct observed upon adsorption of 2 Torr of dioxygen at 298 K. Dotted lines indicate computer simulation of the experimental spectrum. The feature indicated with the asterisk corresponds to the perpendicular component of a residual nickel(I) monocarbonyl species formed during reduction in CO. Much weaker parallel component expected at $g = 2.020$ remains invisible.

for spin−orbit coupling (SOMF), including both the spin-own-orbit and spin-other-orbit interactions in the exchange term.[28] In the spectroscopic calculations the triple-ζ TZP basis set[48] was used for all atoms except for nickel, where a more accurate CP(PPP)[49] basis set was employed. The hyperfine coupling *A* tensor was calculated according to the spin-density-based formulation including the SOC contribution as a second-order propery.[50] For the ^{17}O hyperfine splitting a dedicated EPR-II basis set[51] was used additionally.

3. RESULTS AND DISCUSSION

3.1. Hosting Ni(I) Sites in the MFI Structure. The monovalent nickel centers hosted in ZSM-5 were produced by reduction of the parent Ni^{II}ZSM-5 with CO at 673 K and prolonged evacuation of the reduced samples at 553 K. The monovalent intrachannel nickel(I) centers were produced by reduction of the parent nickel−oxo species following the simple reaction Ni(II)−O−Ni(II) + CO → 2Ni(I) + CO_2.[52] Topological localization of the nickel−oxo and reduced nickel(I) centers within MFI framework (structure of the framework is derived from crystallographic data) is shown in Figure 1.

The corresponding well-resolved, nearly axial EPR spectrum diagnostic of Ni(I) with $g_{zz} > g_{xx,yy}$ is shown in Figure 2a. It consists of two superimposed signals with greatly uneven abundance due to the two types of the topologically different isolated nickel(I) centers with $g_{xx}^1 = g_{yy}^1 = 2.098$, $g_{zz}^1 = 2.487$ and $g_{xx}^2 = g_{yy}^2 = 2.072$, $g_{zz}^2 \cong 2.49$ (the parameters and relative contributions equal to 90% and 8%, respectively, were determined by computer simulation). The feature indicated by the asterisk reveals the presence of a residual nickel(I) monocarbonyl species (with 2% share) that was not destroyed completely by pretreatment in vacuum.[53]

Once the *g*-tensor signatures of the intrazeolite Ni(I) center were extracted reliably, quick screening of its potential locations[34]

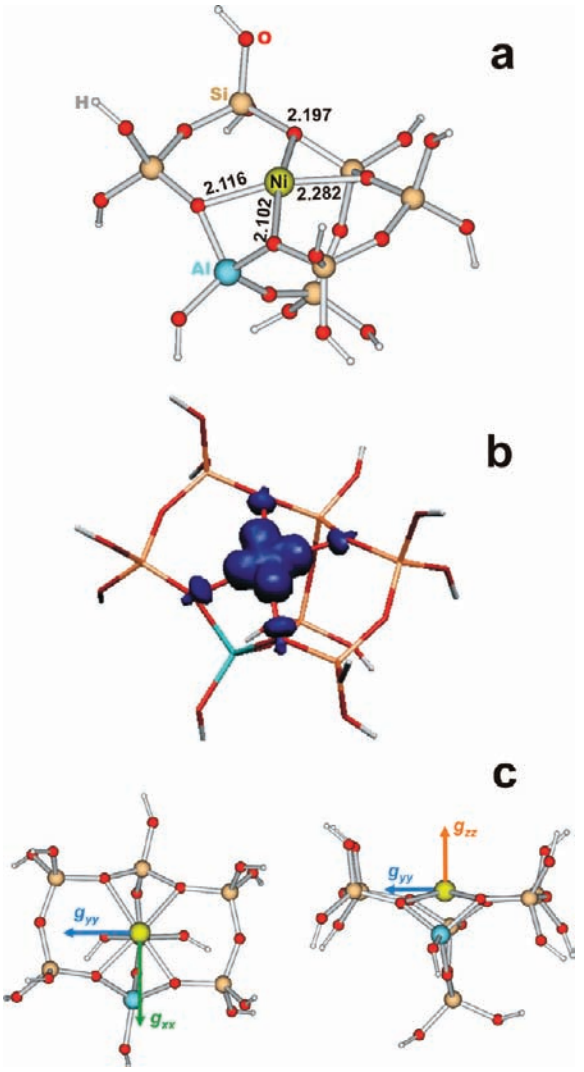

Figure 3. (a) Structure of the Ni^{I}_{4c}**M7** center, (b) corresponding spin-density contour, and (c) orientation of the principal ***g***-tensor axes.

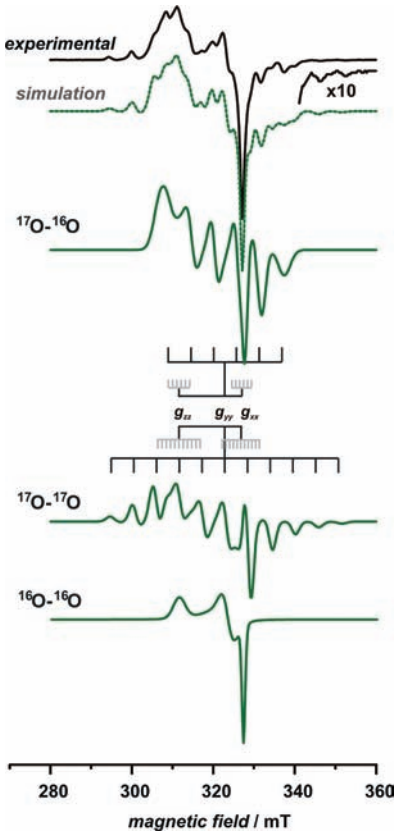

Figure 4. X-band CW-EPR spectrum registered at 77 K of the nickel superoxide adduct observed upon adsorption of 1 Torr of oxygen enriched $^{17}O_2$ at 298 K (dotted line indicates computer simulation of the experimental spectrum). The component signals for the $^{16}O-^{17}O$, $^{17}O-^{17}O$, and $^{16}O-^{16}O$ isotopomers along with the corresponding stick diagram are shown below (the unresolved A_{xx} and A_{zz} hyperfine patterns, assessed by the simulation, are shown in gray).

revealed that only a planar 4-fold environment (with the actual symmetry lowered to C_{2v} by the presence of Al in the framework) gives the results compatible with experiment (see Supporting Information, Table 1S). The tetragonal sites hosting the nickel cations in the ZSM-5 were next modeled using the Ni^{I}_{4c}**M7** cluster of the $Ni^{I}[Si_6AlO_8(OH)_{12}]$ stoichiometry (Figure 3). In the optimized geometry, the nickel(I) center assumes a planar rectangular $Ni^{I}\{O(Si,Al)\}_4$ arrangement ($\Sigma_{\angle O-Ni-O} \cong 354°$) shown in Figure 3a. The Ni−{O(Si,Si)} bond lengths are equal to 2.282 and 2.197 Å, with the corresponding Mayer bond orders of $b_{Ni-O_{Si}} = 0.19-0.22$, whereas the Ni−{O(Al,Si)} bond lengths vary from 2.102 to 2.116 Å ($b_{Ni-O_{Al}} = 0.32$). The Mulliken atomic charge of the Ni center, $q_{Ni} = 0.12$, and the spin density, $\rho_{Ni} \cong 0.94$, are consistent with the monovalent state of the nickel. Indeed, the spin-density repartition is essentially confined to the metal center with a small contribution of the contiguous oxygen donor ligands only (Figure 3b). The calculated (ZORA-SOMF/B3LYP) ***g*** values ($g_{xx} = 2.117$, $g_{yy} = 2.153$, and $g_{zz} = 2.324$) compare well with their experimental counterparts (vide infra). The predicted principal directions of the ***g*** tensor with respect to the molecular framework, with the g_{zz} axis perpendicular to the $Ni^{I}\{O(Si,Al)\}_4$ plane and the in-plane g_{xx} and g_{yy} axes directed between the proximal O(Al,Si) atoms and pointing toward the distal O(Si,Si) atom, respectively, are shown in Figure 3c.

The rhombic distortion of the calculated ***g*** tensor is consistent with the rectangular deformation of the 4-fold arrangement of the planar donor O(Al,Si) ligands caused by the presence of the Al atom in the 12-membered macrocyclic ring. This rhombicity is, however, barely pronounced in the experimental X-band spectrum (Figure 2a). The composition of the SOMO = $0.83|x^2 - y^2\rangle + 0.12|yz\rangle + 0.03|z^2\rangle + 0.01|xz\rangle$ confirms qualitatively the dominant axial component of the ***g*** tensor ($\Delta g_{zz} \approx 8\lambda_{Ni}/(E_{x^2-y^2} - E_{xy})$, $\Delta g_{xx} = \Delta g_{yy} \approx 2\lambda_{Ni}/(E_{x^2-y^2} - E_{xz,yz})$, where λ_{Ni} is a spin−orbit coupling constant and E represents the energy of the corresponding 3d orbitals) associated with the overwhelming $|x^2 - y^2\rangle$ term. The poorly resolved rhombic component can be associated with the appreciable admixture of the $|yz\rangle$ orbital.

The planar structure of the $Ni^{I}\{O(Si,Al)\}_4$ core is reminiscent to that of the biomimetic homogeneous complexes with tetradentate supporting macroligands such as tetraazacycles, Schiff bases, porphyrines,[20,21] and nickel enzymes,[8,9] and as a consequence, similar EPR spectra of Ni(I) were also observed. Yet, the spatial and energetic accessibility of the Ni-based orbitals controlled exclusively by weak oxygen donor ligands in ZSM-5 (discussed below) allows for sufficient activation of the nickel core toward straightforward binding of O_2 molecules.

dx.doi.org/10.1021/ja208387q |*J. Am. Chem. Soc.* 2011, 133, 19931–19943

Table 1. Experimental Spin-Hamiltonian Parameters for Various Heterogeneous and Homogeneous Nickel Superoxide Adducts

	g_{ii} tensor components			^{17}O $\|A_{ii}\|$/mT			
superoxide complex	g_{xx}	g_{yy}	g_{zz}	A_{xx}	A_{yy}	A_{zz}	ref
$(\eta^2$-$O_2)$/NiZSM-5	2.0635	2.0884	2.1675	1.0	5.67	1.3	this work
$(\eta^2$-$O_2)$Ni[PhTt^{Ad}]	2.24	2.19	2.01				23
$[(\eta^1$-$O_2)$[Ni(tmc)](OTf)	2.29	2.21	2.09				21
(O_2)[Ni(dioxo[16]aneN$_5$)]	2.15	2.15	2.02				65
(O_2)[Ni(Ox$_3$)(CH$_3$CN)$_2$(ClO$_4$)$_2$]	2.143	2.143	2.0027				66
$(\eta^2$-$O_2^-)$/MgO	2.0016	2.0083	2.0770	7.63	0.72	0.83	59

3.2. Coordination of Dioxygen to Ni(I) Sites. As mentioned above, the intrazeolite nickel(I) centers provide excellent sites for dioxygen capture at ambient conditions. Adsorption of 2 Torr of $^{16}O_2$ at 298 K on the reduced Ni^{I}ZSM-5 sample led to the development of a new, well-resolved, orthorhombic EPR signal with distinctly different g values (Figure 2b). It can be assigned to a covalently bound superoxide radical,[54] produced following the metal-to-ligand electron transfer (MLET) route

$$^3O_2 + {}^2Ni^IZSM{-}5 \rightarrow {}^2\{Ni^{II}{-}O_2^-\}ZSM{-}5 \qquad (2)$$

As deduced from the changes in the EPR signal intensity with time, the superoxo radical is quite stable at the adsorption temperature (298 K), even upon subsequent evacuation. Upon the same treatment at 373 K it looses about 75% of its initial intensity without reappearance of the EPR signal due to Ni(I), which reveals an irreversible character of O_2 binding.[55]

The corresponding EPR spectrum obtained after reaction with ^{17}O-enriched dioxygen is shown in Figure 4 together with its computer simulation. In accordance with the isotopic composition it consists of two patterns with 6 and 11 lines assigned to the hyperfine structure of the singly $(^{17}O{-}^{16}O)^-$ and doubly $(^{17}O{-}^{17}O)$ labeled isotopomers ($I(^{17}O) = 5/2$), respectively, superimposed on the unstructured signal of the $^{16}O_2^-$ species. The relative weightings of the individual isotopomer signals are 50%, 30%, and 20%, respectively. The clear 11-line pattern associated with the g_{yy} component, well seen at the wings of the spectrum (see the $m_I = \pm 5$ and ± 4 transitions), proves the diatomic nature of the adsorbed species, demonstrating simultaneously that both oxygen nuclei are essentially magnetically equivalent. This fact definitely confirms the "side-on" η^2 geometry of the observed $\{NiO_2\}^{11}$ZSM-5 adduct.

The EPR spectrum of the nickel superoxide species enriched in $^{17}O_2^-$ ($I = 5/2$, 55.5%) was simulated using the following spin-Hamiltonian

$$\mathscr{H} = \beta_e \mathbf{B}^T \cdot g \cdot \mathbf{S} + \mathbf{S}^T \cdot {}^O\mathbf{A} \cdot \mathbf{I} \qquad (3)$$

with $g_{xx} = 2.0635$, $g_{yy} = 2.0884$, $g_{zz} = 2.1675$ and $|{}^OA_{xx}| \leq 1.0 \pm 0.3$ mT, $|{}^OA_{yy}| = 5.67 \pm 0.05$ mT, $|{}^OA_{zz}| \leq 1.3 \pm 0.3$ mT. The quadrupole interaction term ($\boldsymbol{I}^T \cdot \boldsymbol{P} \cdot \boldsymbol{I}$) was neglected in the simulation, since the quadrupole moment of O-17 is small ($Q_O = -0.02558 \times 10^{-28}$ m^2), and its contribution is usually not resolved in powders. Since the A_{xx} and A_{zz} values remain essentially unresolved, giving rise only to the pronounced broadening of the relevant A_{yy} hyperfine lines (Figure 4), their upper values assessed by simulation are biased by larger errors. In this light, the hyperfine parameters were additionally ascertained by DFT calculations (vide supra).

Table 2. Principal Geometric Parameters and Bond Orders for the Intrazeolite η^2-$\{NiO_2\}^{11}$ZSM-5 Adduct[a]

bond length		bond order		bond angles	
$d_{Ni-O_{A1}}$/Å	1.947	$b_{Ni-O_{A1}}$	0.42	$\angle_{O(1)-Ni-O(2)}$	44°
	1.913		0.42		
$d_{Ni-O(1)}$/Å	1.804	$b_{Ni-O(1)}$	0.82	$\angle_{O_{AT}-Ni-O(2)}$	113°
$d_{Ni-O(2)}$/Å	1.796	$b_{Ni-O(2)}$	0.82	$\angle_{O_{AT}-Ni-O_{A1}}$	85°
$d_{O(1)-O(2)}$/Å[b]	1.347	$b_{O(1)-O(2)}$[c]	1.28	$\angle_{O_{AT}-Ni-O(1)}$	117°

[a] Where O(1) and O(2) designate the superoxo atoms. [b] See the bond length in the gas dioxygen, $d_{O-O} = 1.234$ Å, for comparison. [c] See the bond order in the gas dioxygen, $b_{O-O} = 1.94$, for comparison.

It is worth noting here that the extracted EPR parameters of the η^2-$\{NiO_2\}^{11}$ZSM-5 adduct with the reversed g tensor ($g_e < g_{xx}, g_{yy} < g_{zz}, A_{yy} \gg A_{xx}, A_{zz}$) are distinctly different from those previously observed for bioinorganic mono and dihapto analogues ($g_{xx}, g_{yy} > g_{zz}, A_{ii}$ unresolved). They also deviate from those of the side-on O_2^- electrostatic complexes, typified by the classic O_2^-/MgO species with $g_e \approx g_{xx}, g_{yy} < g_{zz}$, and $A_{xx} \gg A_{yy}, A_{zz}$ (Tables 1 and 2). The elucidated unusual magneto-electronic structure of the investigated intrazeolitic species is discussed below.

To recognize a generic structure of the investigated adduct we explored the spectroscopic EPR parameters for a number of conceivable small molecular epitomes such as η^1-$[\{NiO_2\}^{11}$-$(H_2O)_2]^+$, η^2-$[\{NiO_2\}^{11}(H_2O)_2]^+$, $[\{NiO\}^{11}(H_2O)_2]^+$, $[\{ONi$-$O\}^{11}(H_2O)_2]^+$, μ-$\{Ni(\mu$-1,2-$O_2)Ni\}^{19}[(H_2O)_2(OH)]_2$, and μ-η^2:η^2-$[\{O_2Ni_2\}^{19}\{(H_2O)(OH)\}_2]^+$ with various oxygen hapticity (Table 2S, Supporting Information). Only in the case of the η^2-$[\{NiO_2\}^{11}(H_2O)_2]^+$ species the results of the g-tensor calculations were compatible with experiment, allowing for provisional assignment of the observed adduct to the side-on superoxide radical bound to a mononuclear nickel center.[56] Subsequent DFT calculations indicated that, indeed, the most stable ($\Delta E_{ads} = -46.9$ kcal/mol) conformation of the $\{NiO_2\}^{11}$**M7** cluster exhibited the η^2 binding mode of the dioxygen ligand (Figure 5a).

The resulting new planar 4-fold coordination of the metal center is featured by the side-on-ligated superoxide moiety with two slightly inequivalent links to the nickel center (1.804 and 1.796 Å) and two longer Ni−O(Al,Si) bonds equal to 1.947 and 1.913 Å, formed with the zeolite backbone. Apparently, the ligation of dioxygen occurs in a homodesmic way (i.e., preserving the total number of bonds), and new bonds to the coordinated O_2 molecule are formed at the expense of the broken strained Ni−O(Si,Si) connections. Such adsorption mechanism is typical of constraint (entatic) environments and has been previously

dx.doi.org/10.1021/ja208387q |J. Am. Chem. Soc. 2011, 133, 19931–19943

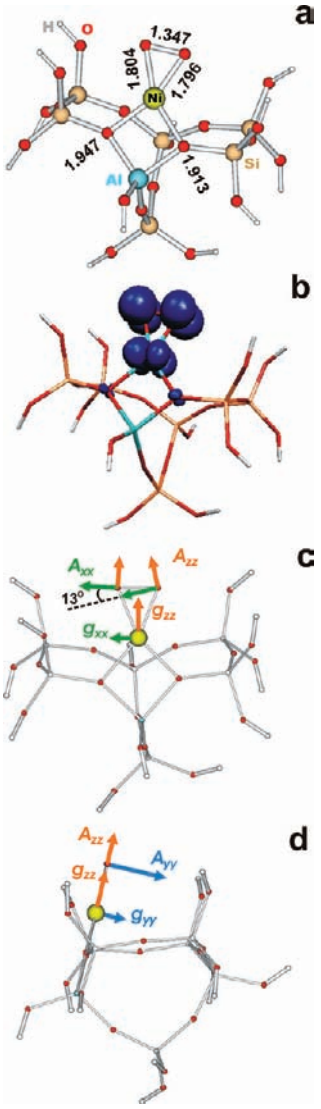

Figure 5. (a) Optimized structure, (b) spin-density contour of the magnetophore, and (c and d) orientation of the principal axes of the ***g*** and (^{17}O) ***A*** tensors for the η^2-$\{NiO_2\}^{11}$**M7** complex. Bond lengths are given in Angstroms and angles in degrees.

observed for NO and CO coordination to metallozeolites.[33] The role of the zeolite structure in formation of the η^2-$\{NiO_2\}^{11}$ species consist of high dispersion and stabilization of the mononuclear nickel(I) centers in the easily accessible sites. The unique bidentate manifold of the supporting oxygen donor ligands, not encountered in biomimetic or organometallic complexes so far, is able to promote straightforward formation of the superoxo nickel complexes.

The interatomic distance, d_{O-O} = 1.347 Å, in the coordinated dioxygen molecule is substantially greater than in the case of the gas-phase O_2 ($^3\Sigma_g$) molecule (d_{O-O} = 1.234 Å), in line with the superoxide formulation of the bound dioxygen (the experimental values were assessed to be in the range of $d_{O-O} \approx$ 1.22–1.36 Å).[57] It compares well with d_{O-O} = 1.347 Å observed in dipodal nickel complexes with the β-diketiminato ligands,[58] indicating a similar activation extent of dioxygen in the case of the O(Si,Al) zeolitic ligands supporting the nickel center, despite the different nature of the donor ligands. The embedded triangular η^2-$\{NiO_2\}^{11}$ moiety exhibits a small bite angle of 44°, essentially the same as in the bare η^2-$\{NiO_2\}^{11}$ species for which d_{O-O} = 1.382 Å was obtained. Upon coordination of dioxygen, the semidetached nickel ion (Ni^{I}_{2c}**M7**) is pushed out of the plane of the zeolite host ring, which is accompanied by the change of the O_{Al}–Ni–O_{Al} angle by 5° and shortening of the Ni–O(Si,Al) bonds by 0.169 and 0.189 Å in comparison to the parent Ni^{I}_{4c}**M7** state. These findings are consistent with the enhanced oxidation state of the Ni center.

The side-on structure of the adduct gives rise to the nearly even triangular spin-density distribution between the superoxide moiety and the nickel core (ρ_{Ni} = 0.36, $\rho_{O(1)}$ = 0.32, $\rho_{O(2)}$ = 0.30), shown in Figure 5b. Changes in the atomic charge distribution upon adsorption within the η^2-$\{NiO_2\}^{11}$ magnetophore (Δq_{Ni} = 0.32, Δq_O = −0.09, Δq_O = −0.11) confirm the MLET mechanism of the dioxygen activation. As a result of strong mixing between the 3d(Ni^{II})–$\pi^*(O_2^-)$ orbitals (discussed below in more detail), the calculated ***g***-tensor values are much larger than those observed for the electrostatically bound O_2^- species.[59] The values obtained within the spin-unrestricted ZORA-SOMF/BP scheme (g_{xx} = 2.039, g_{yy} = 2.098, g_{zz} = 2.178), being in a good agreement with the experiment, prove again the η^2 nature of the observed superoxide species. The orientation of the principal ***g***-tensor axes with respect to the molecular framework of the η^2-$\{NiO_2\}^{11}$**M7** complex is show in Figure 5c and 5d. Both g_{xx} and g_{zz} axes are localized in the $\{NiO_2\}$ plane with the g_{zz} axis bisecting the O–O bond, whereas the g_{yy} alignment is perpendicular to this plane. The hyperfine ^{O}***A*** axes are practically coincident with the ***g*** principal directions. A small deviation (∼13°) of the A_{xx} axis for proximal O-17 atom is experimentally undetectable and may be associated with a small geometrical distortion of the η^2-$\{NiO_2\}$ unit (Figure 5a), which slightly enhances the orbital overlap with the corresponding 3d AO of nickel for this moiety.

3.3. Electronic Structure of the η^2-$\{NiO_2\}^{11}$ Adduct. The electronic structure of the η^2-$\{NiO_2\}^{11}$ZSM-5 adduct was examined in terms of the molecular orbital interactions of the constituting fragments (FMO) defined as the O_2 ligand, the parent tetracoordinated Ni^{I}_{4c}**M7** site, and a virtual "pro-adduct" with the bidentate nickel, referred to as $[Ni^{I}_{2c}$**M7**$]_{fg}$. Since the nickel(I) attachment to the zeolite host changes dramatically upon isodesmic interaction with dioxygen (compare Figures 3a and 5a), the entatic geometry of the $[Ni^{I}_{2c}$**M7**$]_{fg}$ pro-adduct corresponds directly to that of the η^2-$\{NiO_2\}^{11}$**M7** reference complex (with the dioxygen moiety removed) and not to the geometry of the parent tetracoordinated Ni^{I}_{4c}**M7** center. Thus, formation of the η^2-$\{NiO_2\}^{11}$ZSM-5 adduct is factorized into two virtual steps, invoking the $[Ni^{I}_{2c}$/**M7**$]_{fg}$ fragment as a pro-adduct geared up to accommodate the approaching O_2 molecule in a straight way. Such three-fragment approach leads to a more transparent picture of the oxygen bonding, reducing complicated mixing of many orbitals to few key interactions between the meaningful fragment (frontier) orbitals. The orbital overlap correlation diagram of the π^*(2p) states of dioxygen with the 3d states of the $[Ni^{I}_{2c}$**M7**$]_{fg}$ fragment and the parent Ni^{I}_{4c}**M7** cluster is shown in Figure 6.

The energy of dioxygen coordination, computed as the difference between the energies of the η^2-$\{NiO_2\}^{11}$**M7** cluster and both parent fragments, was next factorized into the electrostatic (ΔE_{elect}), steric (ΔE_{steric}), and orbital (ΔE_{orb}) contributions, according to the Morokuma–Ziegler partitioning scheme.[60]

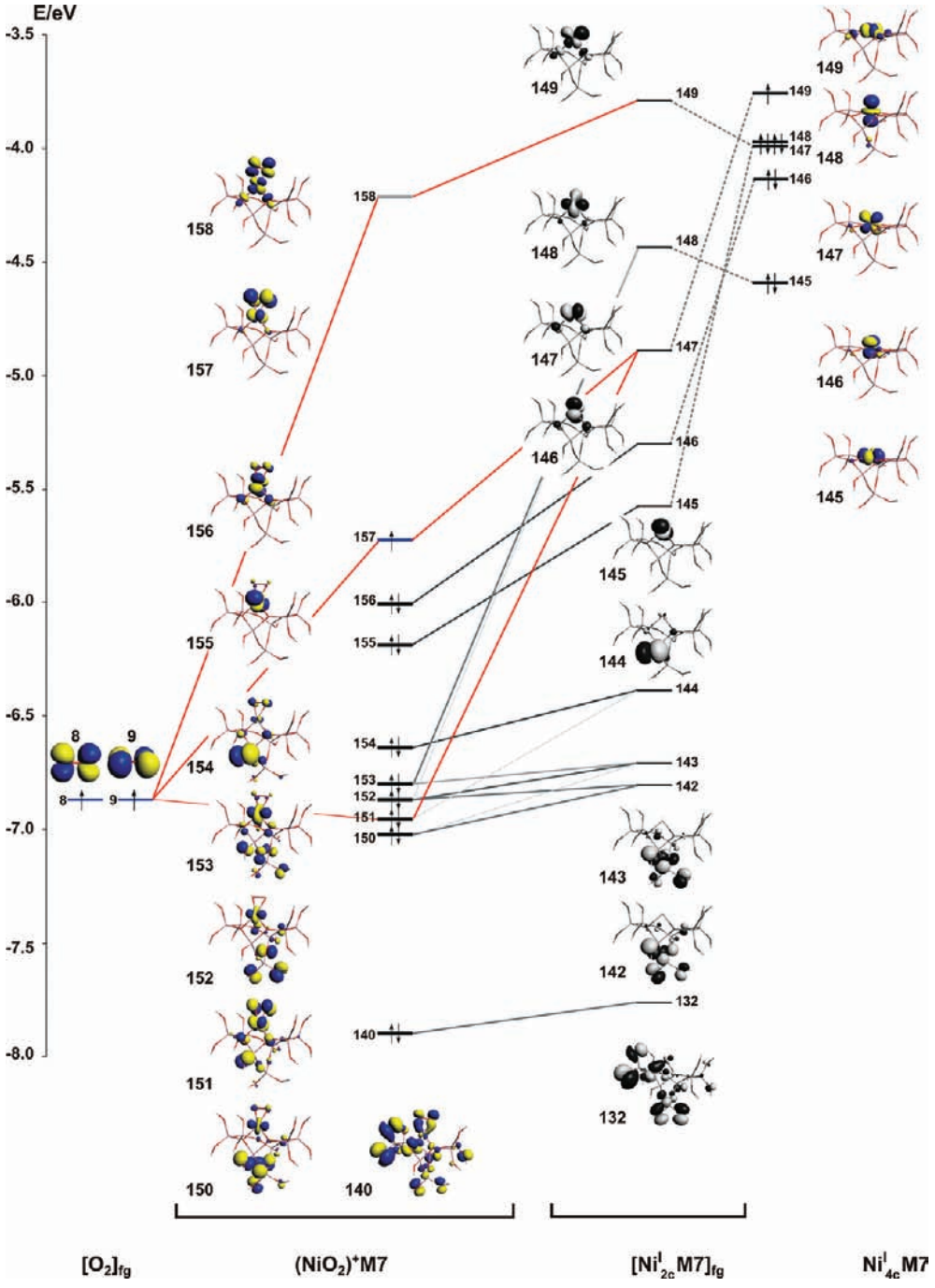

Figure 6. Kohn−Sham orbital interaction diagram for the η^2-$\{NiO_2\}^{11}$**M7** complex.

In the $[Ni^{I}\mathbf{M7}]_{fg}$ pro-adduct state, the change in the nickel coordination results in a significant alteration of the nickel-based d orbitals (Figure 6). In particular, the energy of the **149**($3d_{x^2-y^2}$) level of the Ni^{I}**M7** cluster drops by 1.1 eV, making it energetically more accessible for interaction with the oxygen out-of-plane **9**(π^*2p_x) orbital, whereas that of **147**($3d_{yz}$), exhibiting the same symmetry as the oxygen in-plane **8**(π^*2p_y) state, is moved upward by 0.2 eV. As a result, the semioccupied molecular orbital (SOMO) of the η^2-$\{NiO_2\}^{11}$**M7** adduct originates from the strong interaction between the **9**-(π^*2p_x) level of O_2 and the **147**($3d_{x^2-y^2}$) of the $[Ni^{I}\mathbf{M7}]_{fg}$ fragment, whereas the interaction between the orthogonal **8**(π^*2p_y) and the **149**($3d_{yz}$) levels produce the first virtual **158** state. Such bonding mechanism leads to removal of the degeneracy of both π^*2p orbitals by 1.5 eV, and the frontier orbitals (the δ-antibonding **157** and the π-antibonding **158**) acquire a pronounced metal character. The antibonding frontier **157** and **158** MOs have their bonding counterparts, the **140** and **151** states, respectively, contributing to the binding of dioxygen, since the remaining adjacent orbitals exhibit an essentially nonbonding character toward O_2. The latter are, however, important for molecular interpretation of the ***g*** tensor. Such overlap pattern contributes to the observed unusual increase of the ***g***-tensor anisotropy, discussed below in detail.

dx.doi.org/10.1021/ja208387q |*J. Am. Chem. Soc.* 2011, 133, 19931–19943

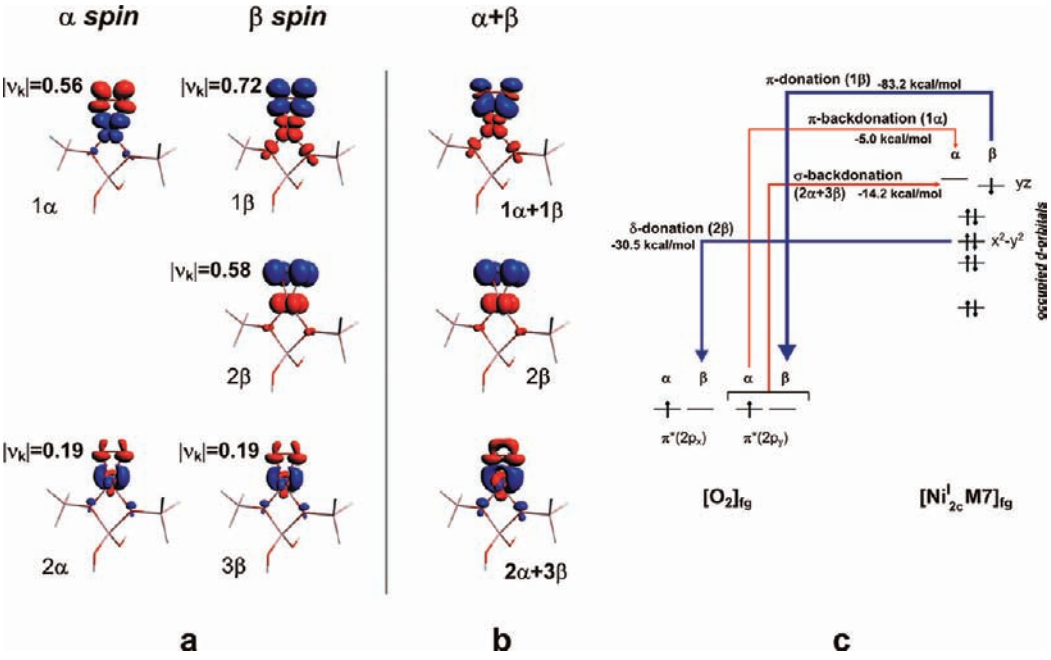

Figure 7. NOCV contours of the deformation density contributions describing the bonding between the dioxygen and the Ni^{I}**M7** site for the (a) α and β spin orbitals and (b) cumulative contours ($\alpha + \beta$); (c) corresponding energy diagram showing the flow channels and associated orbital energies. Blue and red contours correspond to gain and loss of the electron density, respectively.

The sizable destabilizing ΔE_{steric} part of the interaction energy between O_2 and Ni^{I}**M7** arises from the Pauli repulsive interaction (+ 890.7 kJ/mol) between the closed-shell orbitals of both fragments. Although this effect is significantly attenuated by the favorable electrostatic interactions within the $\{Ni^{II}-O_2^{-}\}$ moiety ($\Delta E_{elect} = -366.4$ kJ/mol), the overall constructive binding effect is assured by substantial orbital component ($\Delta E_{orb} = -591.7$ kJ/mol), discussed above.

As revealed by the Mulliken population analysis and the ample electrostatic part of the interaction energy, the adsorbed O_2 moiety accumulates a negative net charge consistent with its radical O_2^{-} character. This partial charge arises from the balance between the metal-to-ligand (donation) and the ligand-to-metal (back-donation) flows of the electron density within the $\{NiO_2\}^{11}$ unit. Yet, the resultant charge density repartition is not necessarily congruent with the associated spin-density flow. The confluence and divergence of these processes was resolved by means of ETS-NOCV analysis, and the specific charge and spin flow channels were identified and quantified in terms of their energetic relevance. Within the decomposition scheme into the $[O_2]_{fg}$ and $[Ni^{I}_{2c}\mathbf{M7}]_{fg}$ fragments, the main contributions ($|\nu_k| > 0.1$) to the α and β electron density flows are shown in Figure 7, along with the corresponding ΔE_{orb} values. They are categorized into the σ, π, and δ channels, defined by the overlap symmetry of the involved orbitals.

A π channel of the incongruent charge−spin-density flow, a charge density flow σ channel, and a δ channel of the congruent charge−spin-density flow was identified. A pair of spin orbitals with the prime contribution to the orbital interaction energy is represented by 1α and 1β deformation densities. They correspond to the spin-polarized π-donation (1β) and π-backdonation (1α) processes (Figure 7a) of the highly uneven energetic contributions equal to −83.2 and −5.0 kcal/mol (Figure 7c), respectively. As a result, the weighted sum of the densities ($1\alpha + 1\beta$) shows a net charge and β spin flows of the π-donation nature, which occur from the β-$3d_{yz}$ nickel state (hybridized with the framework oxygen donor atoms) to the antibonding $\beta-\pi^*$-($2p_y$) spin orbital of dioxygen (Figure 7c). The charge backdonation effect is slightly enhanced by the spinless transfer of the considerable charge density ($|\nu_k| = 0.19$) from $\pi^*(2p_y)$ to d_{yz} through the σ channel ($2\alpha + 3\beta$), associated with a rather small energy gain of −14.2 kcal/mol. The δ-donation channel (2β) operates only within the β-spin states (Figure 7a) and refers to the interaction of −30.5 kcal/mol between the $3d_{x^2-y^2}$ orbital of nickel and the antibonding $\pi^*(2p_x)$ MO of dioxygen, constituting the SOMO (Figure 6). Since only one β-spin manifold is involved herein, this channel can be identified with the congruent charge−spin transfer process. As a result, ETS-NOCV analysis revealed substantial electron and spin-density redistribution through σ, π, and δ channels upon the interaction of O_2 with the Ni^{I} sites. Two partly counterbalancing π channels (β-polarized donation and α-polarized backdonation), reinforced by a small charge-only σ-backdonation, and a concerted charge−spin δ donation of β polarization, acting cooperatively in

Table 3. Relativistic DFT Calculations of the Spin-Hamiltonian Parameters for the η^2-$\{q^{2+}-O_2^{-}\}^3$ and η^2-$\{NiO_2\}^{11}$ Adducts

		g tensor		
adduct type	calculation scheme	g_{xx}	g_{yy}	g_{zz}
η^2-$\{q^{2+}-O_2^{-}\}^3$	Pauli/BP	2.002	2.012	2.079
η^2-$\{NiO_2\}^{11}$	Pauli/BP	2.025	2.046	2.118
	ZORA-SOMF/BP	2.036	2.049	2.141
η^2-$\{NiO_2\}^{11}$**I2**	Pauli/BP	2.042	2.106	2.181
	ZORA-SOMF/BP	2.039	2.096	2.174
η^2-$\{NiO_2\}^{11}$**M7**	Pauli/BP	2.042	2.105	2.188
	ZORA-SOMF/BP	2.039	2.098	2.178

dx.doi.org/10.1021/ja208387q |*J. Am. Chem. Soc.* 2011, 133, 19931–19943

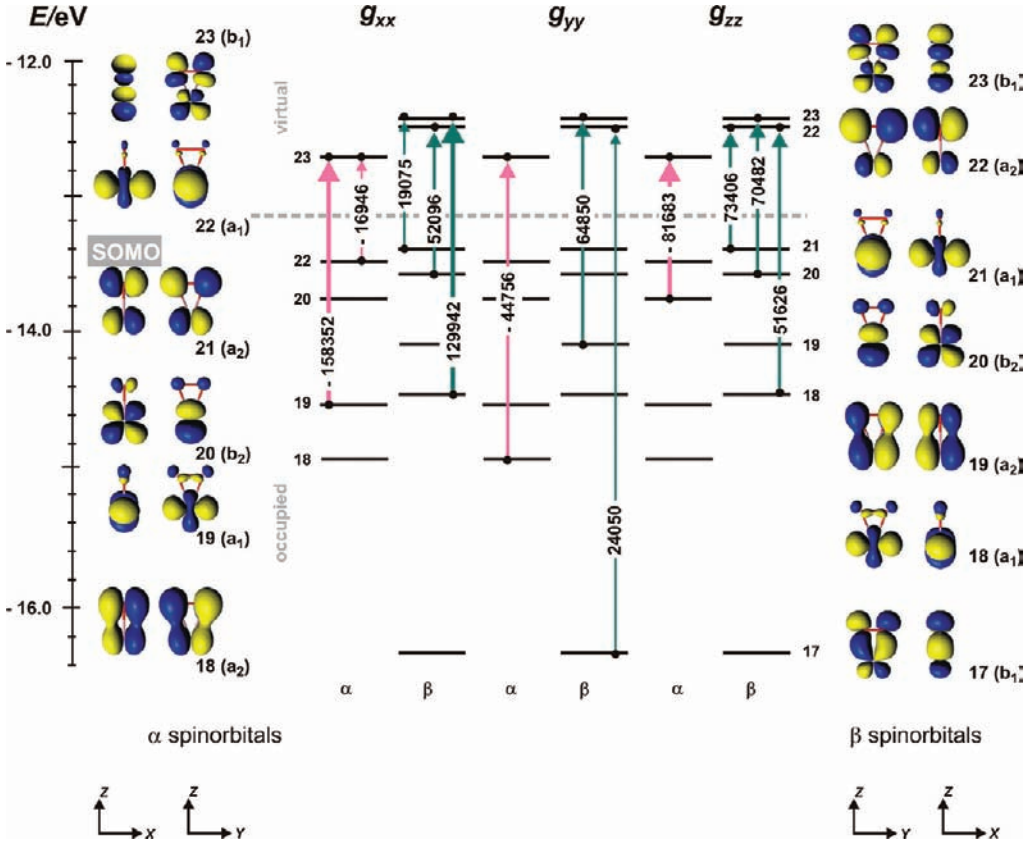

Figure 8. Kohn−Sham orbital diagram for the most important paramagnetic contributions to the *g*-tensor components of the model η^2-$\{NiO_2\}^{11}$ unit in the spin-unrestricted BP/TZP scalar relativistic calculations based on the Pauli Hamiltonian. Magnetic field-induced couplings are indicated with arrows, whereas the corresponding contributions (>10%) are given in ppm.

formation of the nickel-bound superoxo O_2^- radical, were ascertained for the first time. The magnetic features of the η^2-$\{Ni^{II}-O_2^-\}^{11}$ unit, defined by the metal-to-ligand β-spin-density transfer through the δ and π channels, give rise to the fairly uniform redistribution of the spin density within the superoxo−nickel moiety (Figure 5b).

3.4. Molecular Interpretation of the *g* Tensor. Quantitative reproduction of the *g* tensor for the η^2-$\{NiO_2\}^{11}$ZSM-5 adduct and its molecular epitoms was achieved by the relativistic DFT calculations based on the ZORA, SOMF, and Pauli Hamiltonian approach, and the results are summarized in Table 3.

The calculated g_{ii} components were rationalized in terms of the individual Kohn−Sham orbital contributions, according to the partitioning scheme implied by the scalar Pauli Hamiltonian

$$\Delta g_{ij} = \Delta g_{ij}^{rel} + \Delta g_{ij}^{d} + \Delta g_{ij}^{p} \quad (4)$$

where Δg_{ij}^{rel} combines scalar relativistic corrections whereas the terms Δg_{ij}^{d} and Δg_{ij}^{p} stand for dia- and paramagnetic contributions to Δg_{ij}, respectively. The corrections due to the relativistic and diamagnetic effects are below 1% for η^2-$\{q^{2+}-O_2^-\}^3$ and 3% for the bare η^2-$\{NiO_2\}^9$. As observed earlier,[61,62] the paramagnetic term (Δg_{ij}^{p}) dominates deviation of the *g*-tensor elements from the free electron value; therefore, while analyzing the molecular nature of the *g*-tensor anisotropy we restrict our discussion to this overwhelming term only. The main contributions to Δg_{ij}^{p} are defined by the magnetic field-induced couplings between the occupied and virtual orbitals ($\Delta g_{ij}^{p,occ\text{-}virt}$), accounting for more than 90% of the total shift, which can be deduced from the non-vanishing elements of the following integrals[61]

$$\Delta g_{ij}^{p,\,m\,-\,n} \propto \frac{1}{2c(\varepsilon_n^\sigma - \varepsilon_m^\sigma)} \langle \Psi_m^\sigma | iL_{i=x,y,z} | \Psi_n^\sigma \rangle \quad (5)$$

where Ψ_m and Ψ_n are the unperturbed Kohn−Sham orbitals, ε is the one-electron energy, $L_{i=x,y,z}$ is the orbital momentum operator, whereas σ stands for α or β spin. To simplify the diagrams only the most important contributions (exceeding 10% of the total Δg) were taken into account.

To disentangle explicit orbital contributions to the observed *g*-tensor anisotropy resulting from the magnetic interactions within the nickel−superoxide unit from those associated with its bonding to the zeolitic framework, a discrete covalent η^2-$\{Ni^{II}-O_2^-\}^{11}$ and a purely electrostatic η^2-$\{q^{2+}-O_2^-\}^3$ reference models were analyzed at first. In the latter case, the DFT calculations can be compared directly with the widely used semiempirical treatment of the *g* tensor of bound O_2^- ($^2\Pi_{3/2}$) species developed by Känzing and Cohen.[63]

As shown by the spin-restricted Pauli calculations even for the simplest electrostatic η^2-$\{q^{2+}-O_2^-\}^3$ epitome of C_{2v} point symmetry (see the Supporting Information, Figure 1Sa), the obtained results (g_{xx} = 2.002, g_{yy} = 2.012, g_{zz} = 2.079) are in good agreement with the experimental data observed for the real η^2-O_2^-/MgO system (Table 1). Within the calculation accuracy, the g_{xx} value remains intact (in the C_{2v} point group the spin−orbit coupling of the SOMO with the $9b_1(\pi_x^*)$ and $6a_1(\sigma_{2p})$ states is forbidden for L_x by symmetry), whereas the

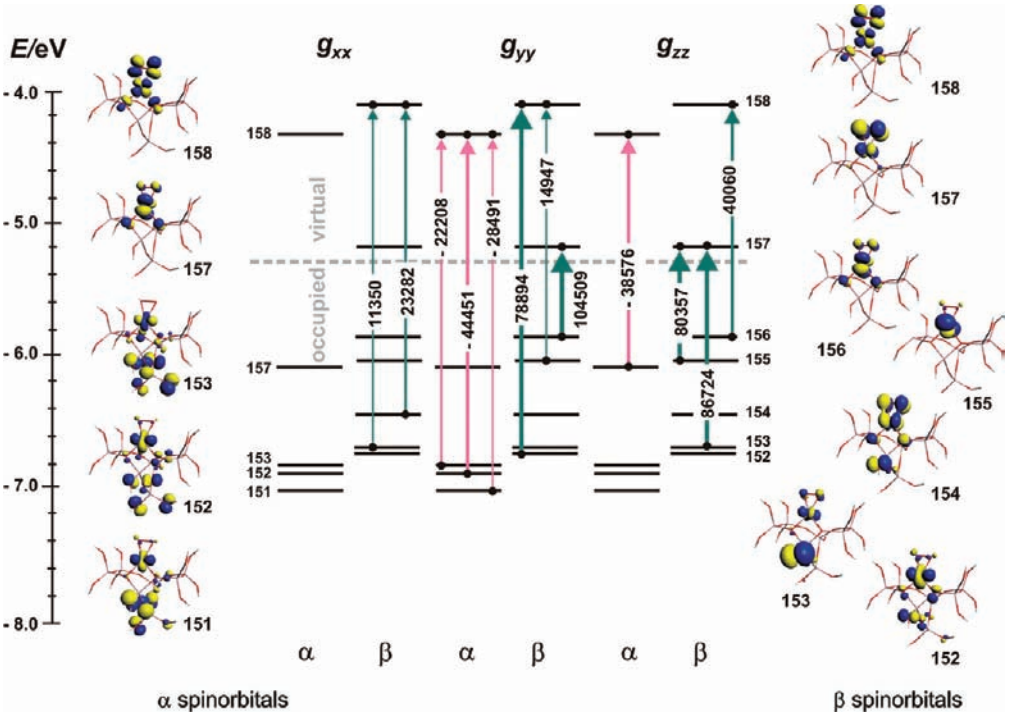

Figure 9. Kohn−Sham orbital diagram for the most important paramagnetic contributions to the *g*-tensor components of the η^2-$\{NiO_2\}^{11}$**M7** cluster in the spin-unrestricted BP/TZP scalar relativistic calculations based on the Pauli Hamiltonian. Magnetic field-induced couplings are indicated with arrows, whereas the corresponding contributions (>10%) are given in ppm.

g_{yy} component is affected by one small coupling between the occupied **6**$a_1(\sigma_{2p})$ and the semioccupied **9**$b_1(\pi_x^*)$ orbitals. The shift of the most sensitive g_{zz} component arises from one strong coupling between the **8**$b_2(\pi_y^*)$ and **9**$b_1(\pi_x^*)$ MOs. Such coupling scheme provides a detailed molecular rational for the $g_{zz} \gg g_{yy} > g_{xx} \approx g_e$ sequence (predicted also by the Känzing and Cohen treatment), which has been experimentally observed for most of the bound superoxo species on ionic surfaces, where the simple crystal field account is valid.[54]

In comparison to the electrostatically attached O_2^- radicals, all the *g*-tensor components of the η^2-$\{NiO_2\}^{11}$ZSM-5 adduct are substantially shifted toward higher values and the *g*-tensor anisotropy increases considerably. This is the consequence of not only a direct involvement of the nickel-based states into the magnetic couplings but, for the most part, of the appearance of new transitions revealed by analysis of the corresponding molecular diagram for the discrete η^2-$\{NiO_2\}^{11}$ unit (Supporting Information, Figure 1Sb). The g_{xx} component (equal to g_e in the electrostatic model) is now affected by two moderate couplings **17**$b_2(d_{xz}+\pi^*)$ ↔ **22**$a_2(d_{x^2-y^2}-\pi^*)$ and **22**$a_2(d_{x^2-y^2}-\pi^*)$ ↔ **23**$b_2(d_{xz}-\pi^*)$, whereas the Δg_{yy} shift is dominated by the **20**$b_1(d_{yz}-\pi^*)$ ↔ **22**$a_2(d_{x^2-y^2}-\pi^*)$ coupling. The contributions to the g_{zz} value include two strong **21**$a_1(d_{z^2}-\pi^*)$ ↔ **22**a_2-$(d_{x^2-y^2}-\pi^*)$ and **18**$a_1(d_{z^2}-\sigma)$ ↔ **22**$a_2(d_{x^2-y^2}-\pi^*)$ magnetic transitions. Thus, all g_{ii} components acquire a pronounced mixed metal−ligand nature involving mostly the couplings of the SOMO with the occupied states. This explains qualitatively large positive shifts of all *g*-tensor components for the η^2-$\{NiO_2\}^{11}$ magnetophore and their distinctly different molecular character in comparison to the electrostatic η^2-$\{q^{2+}-O_2^-\}^3$ analogue (Table 1).

Although the spin-restricted calculations provide a lucid account of the *g*-tensor anisotropy based on the magnetic couplings of the occupied orbitals with the SOMO (which conceptually is close to the classic semiempirical treatment based on the second-order perturbation theory), more adequate spin-unrestricted calculations with the Pauli Hamiltonian yield g_{ii} values (g_{xx} = 2.025, g_{yy} = 2.046, g_{zz} = 2.118) that are in a much better agreement with experiment. The corresponding magnetic couplings between the α and the β spin orbitals shown in Figure 8 reveal the complex nature of all *g*-tensor components associated with the uneven paramagnetic α and β currents.

Thus, the g_{xx} value is dictated by the β-**20**$b_2(d_{xz}-\pi^*)$ ↔ β-**22**$a_2(d_{x^2-y^2}-\pi^*)$ transition, since the remaining β-**18**$a_1(d_{z^2}-\sigma)$ ↔ β-**23**$b_1(d_{yz}-\pi^*)$ and β-**21**$a_1(d_{z^2}-\pi^*)$ ↔ β-**23**$b_1(d_{yz}-\pi^*)$ couplings are nearly counterbalanced by the α-**19**$a_1(d_{z^2}-\sigma)$ ↔ α-**23**$b_1(d_{yz}-\pi^*)$ and α-**22**$a_1(d_{z^2}-\pi^*)$ ↔ α-**23**$b_1(d_{yz}-\pi^*)$ transitions. In the case of the g_{yy} component, the β-**19**$a_2(d_{x^2-y^2}+\pi^*)$ ↔ β-**23**$b_1(d_{yz}-\pi^*)$ coupling is attenuated by the α-**18**a_2-$(d_{x^2-y^2}+\pi^*)$ ↔ α-**23**$b_1(d_{yz}-\pi^*)$ one but the overall Δg_{yy} shift is reinforced by the β-**17**$b_1(d_{yz}+\pi^*)$ ↔ β-**22**$a_2(d_{x^2-y^2}-\pi^*)$ transition. For the g_{zz} component, the negative α-**20**$b_2(d_{xz}-\pi^*)$ ↔ α-**23**$b_1(d_{yz}-\pi^*)$ transition is compensated by the positive β-**20**$b_2(d_{xz}-\pi^*)$ ↔ β-**23**$b_1(d_{yz}-\pi^*)$ one, leaving the two other β-**18**$a_1(d_{z^2}-\sigma)$ ↔ β-**22**$a_2(d_{x^2-y^2}-\pi^*)$ and β-**21**$a_1(d_{z^2}-\pi^*)$ ↔ β-**22**$a_2(d_{x^2-y^2}-\pi^*)$ strong contributions (analogous to those observed in the spin-restricted scheme) to account for the observed largest shift in this direction. Despite the rather complex nature of the involved magnetic couplings, for each g_{ii} component it is possible to distinguish one or two dominating transitions of metal−ligand character, as the remaining transitions suppress each other in the α and β spin currents to a large extent.

Modification of the molecular picture of the *g* tensor upon embedding into the zeolite host was examined using the η^2-$\{NiO_2\}^{11}$**M7** model (of the C_1 point symmetry). Similar

Table 4. Comparison of the Experimental and DFT-Calculated Hyperfine Coupling Constants for the η^2-$\{NiO_2\}^{11}$ZSM-5 Adduct Together with Atomic Spin Densities Derived from Analysis of the ^{O}A Tensor

hyperfine tensor		A_{xx}/MHz	A_{yy}/MHz	A_{zz}/MHz	A_{iso}/MHz
experiment		(+)28.88	(−)165.7	(+)39.44	(−)32.46
ZORA-SOMF/B3LYP[a]					
η^2-$\{NiO_2\}^{11}$**M7**	O (1)	32.16	−189.41	33.83	−41.14
	A_{FC}	−36.17	−36.17	−36.17	
	A_{SD}	69.50	−153.32	83.82	
	A_{SO}	−1.17	0.08	−13.82	
	O (2)	29.29	−179.89	30.60	−40.00
	A_{FC}	−35.25	−35.25	−35.25	
	A_{SD}	70.03	−144.72	74.69	
	A_{SO}	−5.48	0.08	−8.84	

		EPR			DFT		
atomic spin densities (%)		ρ_s	ρ_π^x	ρ_π^y	ρ_s	ρ_π^x	ρ_π^y
	O (1)	0.6	2.1	40.6	0.8	0.1	40.8
	O (2)	0.6	2.1	40.6	0.8	0.2	38.2

[a] EPR-II basis set on oxygen, CP(PPP) basis set on nickel, and TZV all other atoms.

to the previously investigated η^1-$\{CuNO\}^{11}$ and η^1-$\{NiCO\}^9$ species,[34,62] the nickel-bound superoxo moiety is also quite sensitive to the perturbation induced by the zeolite host. The g_{zz} component is gauged by one α and three β couplings (α-**157**($d_{xz}-\pi^*$) ↔ α-**158**($d_{yz}-\pi^*$), β-**155**($d_{z^2}-\pi^*$) ↔ β-**157**($d_{x^2-y^2}-\pi^*$), β-**153**($d_{x^2-y^2}-\pi^*$) ↔ β-**157**($d_{x^2-y^2}-\pi^*$), and β-156($d_{xz}-\pi^*$) ↔ β-**158**($d_{yz}-\pi^*$)) that are analogous to those observed in the bare η^2-$\{NiO_2\}^{11}$ unit, modified by an admixture of the framework ligand-based orbitals (Figure 9). Among them, only the β-**156**($d_{xz}-\pi^*$) ↔ β-**158**($d_{yz}-\pi^*$) transition is sensitive to the structure of the local environment, owing to the noticeable contributions of the oxygen framework orbitals. A similar situation occurs for the g_{yy} component, where three α and three β mutually opposing magnetic transitions (α-**153**($d_{z^2}-\sigma$) ↔ α-**158**($d_{yz}-\pi^*$), α-**152**($d_{z^2}-\sigma$) ↔ α-**158**($d_{yz}-\pi^*$), α-**151**($d_{z^2}-\sigma$) ↔ α-**158**($d_{yz}-\pi^*$) and β-**152**($d_{z^2}-\sigma$) ↔ β-**158**($d_{yz}-\pi^*$), β-**155**($d_{z^2}-\pi^*$) ↔ β-**158**($d_{yz}-\pi^*$), β-**156**($d_{xz}-\pi^*$) ↔ β-**157**($d_{x^2-y^2}-\pi^*$)) involve orbitals with a considerable share of the framework ligands. Again, the relatively strong β-**152**($d_{z^2}-\sigma$) ↔ β-**158**($d_{yz}-\pi^*$) coupling may account for the structure sensitivity of this component. In the case of the g_{xx} value, the coupling scheme is much simplified, since only two β transitions (β-**153**($d_{x^2-y^2}-\pi^*$) ↔ β-**158**($d_{yz}-\pi^*$) and β-**154**($d_{x^2-y^2}+\pi^*$) ↔ β-**158**($d_{yz}-\pi^*$)) with the contributions exceeding the threshold value of 10% can be distinguished. As a result, the Δg_{xx} shift is the smallest one and, therefore, structurally less informative.

Thorough analysis of the $\boldsymbol{g}$ tensor of the η^2-$\{NiO_2\}^{11}$**M7** adduct revealed its distinctly different character in comparison to the already discussed electrostatic congener (O_2^-/MgO) and biomimetic analogues (Table 1). Being formally described as η^2 nickel(II) superoxide species, it exhibits significantly different electronic and magnetic structure. In the case of the homogeneous oxygen adducts with nickel complexes the typical bonding situation is based on the spin-pairing mechanism, effected by the overlap of the singly occupied Ni $3d_{x^2-y^2}$ with the in-plane oxygen $2p(\pi^*)$ orbitals. The SOMO is then dominated by the nickel $3d_{z^2}$ orbital, giving rise to the rhombic $\boldsymbol{g}$ tensor with $g_{zz} \ll g_{xx}, g_{yy}$ (see Table 1). Such situation differs dramatically from that observed for the investigated intrazeolitic η^2-$\{NiO_2\}^{11}$ZSM-5 nickel dioxygen adducts. Here, the SOMO is produced by δ overlap of the nickel $3d_{x^2-y^2}$ with the out-of-plane oxygen $2p(\pi^*)$ orbitals, which allows for congruent charge and spin metal-to-ligand density flow, giving rise to the unique triangular magnetophore with nearly even spin-density repartition within the η^2-$\{NiO_2\}^{11}$ unit. Thus, dissimilar magnetic structure in both cases can be accounted for by the different mechanism of dioxygen binding based on a coupled spin and electron transfer in the case of intrazeolite adducts and on a spin pairing for homogeneous and biomimetic complexes.

3.5. O-17 Hyperfine Coupling Tensor. As already discussed (section 3.2) the ^{17}O hyperfine pattern confirms definitely the side-on coordination of the η^2-$\{NiO_2\}^{11}$ZSM-5 adduct. Although only the diagnostic A_{yy} splitting was well resolved, the values of the remaining A_{xx} and A_{zz} splittings were assessed with acceptable accuracy by computer simulation.

To analyze the spin-density distribution associated within the superoxo moiety (i.e., on the 2σ, π_x, and π_y orbitals involved in the SOMO), the ^{O}A tensor can be decomposed into the isotropic (a_{iso}) and dipolar ($\boldsymbol{T}$) terms, $^{O}\boldsymbol{A} = a_{iso} + \boldsymbol{T} = a_{iso} + \boldsymbol{B}_y + \boldsymbol{B}_x$, in the following way

$$
{}^{o}A/\mathrm{MHz} = \begin{bmatrix} +28.88 & & \\ & -165.7 & \\ & & +39.44 \end{bmatrix}
$$

$$
= -32.46 + \begin{bmatrix} +68.38 & & \\ & -136.8 & \\ & & +68.38 \end{bmatrix}
$$

$$
+ \begin{bmatrix} -7.04 & & \\ & +3.52 & \\ & & +3.52 \end{bmatrix}
$$

where the first and second matrix are related to decomposition along the y ($\boldsymbol{B}_y$) and x ($\boldsymbol{B}_x$) axes, respectively. In this parametrization $\boldsymbol{B}$ includes both the dipolar ($\boldsymbol{A}_{SD}$) and the second-order spin−orbit ($\boldsymbol{A}_{SO}$) contributions. The experimental value of a_{iso} = −32.46 MHz is in line with the dominant spin polarization found earlier for the ionic O_2^- radicals trapped on MgO surfaces (a_{iso} = −60.7 MHz).[59] The less negative value, as compared with the O_2^-/MgO paramagnet, can be reconciled with a sizable shift of the spin density from the superoxo moiety to the nickel core (Figure 5b), which is discussed in section 3.3.

Using the reported atomic value for the dipolar ^{17}O hyperfine constant, $B_0 = 4/5P_d = -336.8$ MHz,[64] experimental atomic spin density on the oxygen $2p\pi^y$ and $2p\pi^x$ orbitals was assessed by classic treatment applying the formula $\rho_\pi^i = B_i/B_0$, where B_x = −7.04 MHz and B_y = −136.8 MHz. In the same way spin-density repartition on the 2s orbital, $\rho_s = a_{iso}/A_0$, was calculated using the A_0 value of −5263 MHz.[64] The obtained results listed in Table 4 confirm that the spin density on the superoxide moiety is largely confined to the π_y state, and the admixture of the orthogonal π_x state is small.

The experimental values of the hyperfine a_{iso} and T_{ii} coupling constants were next corroborated by the relativistic DFT

calculations using the ZORA-SOMF/B3LYP scheme. The results are summarized in Table 4, and the relative orientations of the principal hyperfine axes with respect to the g-tensor directions are shown in Figure 5c and 5d. For the TZV(P) and EPR-II basis sets tested for the oxygen atoms the obtained results were virtually equivalent. The calculated A_{ii} values nicely agree with their experimental counterparts, especially for the unresolved A_{xx} and A_{zz} directions, reinforcing the credibility of the fit of the observed EPR spectrum (Figure 4). Furthermore, the experimental atomic spin densities agree well with that derived from DFT population analysis.

By applying coupled-perturbed Kohn−Sham theory, the calculated hyperfine coupling constants were factorized into Fermi-contact (A_{FC}), dipolar (A_{SD}), and second-order spin−orbit (A_{SO}) contributions.[50] Although the present calculations involve light ^{17}O nuclei, the last term can be of significance because of the large spin density accommodated on the superoxo ligand. Analysis of the individual contributions to the ^{17}O hyperfine tensor (Table 4) revealed clear hierarchy of their significance. The spin−dipolar part predominates in magnitude, the negative A_{FC} Fermi-contact term accounts for less than 50% of A_{SD}, whereas the A_{SO} spin−orbit contribution is on the order of tens of MHz. Since A_{SO} is proportional to Δg, the calculated second-order contribution is biggest for the A_{zz} component as it can actually be seen in Table 4.

4. CONCLUSIONS

By means of the combined use of EPR, isotopically enriched oxygen-17, and relativistic DFT molecular modeling it was shown that interaction of dioxygen with Ni^{I}ZSM-5 zeolite led to formation of the side-on superoxide adduct of nickel(II) with unprecedented magnetic structure ($g_e < g_{xx}, g_{yy} < g_{zz}$, $|A_{yy}| \gg |A_{xx}|, |A_{zz}|$) as compared to the corresponding biomimetic analogues. Ligation of dioxygen occurs in a homodesmic way typical of constraint environments. The components of the g and $A(^{17}O)$ tensors ($g_{xx} = 2.0635, g_{yy} = 2.0884, g_{zz} = 2.1675$, and $|A_{xx}| \approx 1.0$ mT, $|A_{yy}| = 5.67$ mT, $|A_{zz}| \approx 1.3$ mT) were well reproduced by ZORA-SOMF calculations, confirming the structure assignment definitely. The detailed molecular nature of the g tensor and its structure sensitivity were discussed in terms of the molecular orbital contributions due to the magnetic field-induced couplings, obtained within the scalar relativistic Pauli Hamiltonian approximation. The charge and spin-density redistributions within the η^2-$\{NiO_2\}^{11}$ magnetophore were analyzed be means of the ETS-NOCV method. It has been shown that three distinct channels of the spin and charge density flow of π, σ, and δ symmetry act cooperatively in formation of the superoxo species. The π channel allows for the incongruent charge and spin-density donation, the σ channel is responsible for the charge-only back-donation, whereas the δ channel, operating only within the β spin orbitals, enables the congruent charge and spin-density flow. The revealed flows lead jointly to the nearly homogeneous distribution of the spin density within the η^2-$\{NiO_2\}^{11}$ unit. To the best of our knowledge, the η^2-$\{NiO_2\}^{11}$ superoxo adducts have not been observed yet for digonal mononuclear nickel(I) centers supported by oxygen donor ligands.

■ ASSOCIATED CONTENT

Ⓢ Supporting Information. DFT (ZORA-SOMF) calculated g tensor and O-17 hyperfine coupling constants for model nickel(I) and nickel(II)−superoxo complexes; Kohn−Sham orbital diagram of paramagnetic contributions to the g-tensor components of the η^2-$\{q^{2+}-O_2\}^3$ and η^2-$\{NiO_2\}^{11}$ units; simulation of the EPR spectrum of Ni^{I}ZSM-5 sample; DFT geometry-optimized Cartesian coordinates of the η^2-$\{NiO_2\}^{11}$-M7 complex in *xyz* format. This material is available free of charge via the Internet at http://pubs.acs.org.

■ AUTHOR INFORMATION

Corresponding Author
pietrzyk@chemia.uj.edu.pl.

■ ACKNOWLEDGMENT

Financial support by the Ministry of Science and Higher Education (MNiSW) of Poland, Grant No. N N204 239334, is acknowledged. P.P. is grateful to the Ministry for the Young Scientists' Stipend. T.M. is thankful for support from the International PhD studies program at the Faculty of Chemistry, Jagiellonian University, within the MPD Program of the Foundation for Polish Science cofinanced by the EU Regional Development Fund. This research was carried out with the equipment partly purchased thanks to the financial support of the European Regional Development Fund in the framework of the Polish Innovation Economy Operational Program (contract no. POIG.02.01.00-12-023/08). We also thank Professor Michel Che from the University of Pierre and Marie Curie, Paris VI, for granting us the O-17-enriched oxygen.

■ REFERENCES

(1) Ozin, G. A.; Gil, C. *Chem. Rev.* **1989**, *89*, 1749–1764.
(2) Thomas, J. M. *Angew. Chem., Int. Ed.* **1999**, *38*, 3588–3628.
(3) Corma, A. *Catal. Rev.- Sci. Eng.* **2004**, *46*, 369–417.
(4) Derouane, E. G. *A Molecular View of Heterogeneous Catalysis*; Derouane, E. G., Ed.; De Boeck & Larcier SA: Paris, 1998; Chapter 1, p 5.
(5) Tinberg, C. E.; Lippard, S. J. *Acc. Chem. Res.* **2011**, *44*, 280–288.
(6) Groothaert, M. H.; van Bokhoven, J. A.; Battiston, A. A.; Weckhuysen, B. M.; Schoonheydt, R. A. *J. Am. Chem. Soc.* **2003**, *125*, 7629–7640.
(7) Chen, P.; De Beer George, S.; Cabrito, I.; Antholine, W. E.; Moura, J. J. G.; Moura, I.; Hedman, B.; Hodgson, K. O.; Solomon, E. I. *J. Am. Chem. Soc.* **2002**, *124*, 744–745.
(8) Eckert, N. A.; Dinescu, A.; Cundari, T. R.; Holland, P. L. *Inorg. Chem.* **2005**, *44*, 7702–7704.
(9) Frey, M. *Struct. Bonding (Berlin)* **1998**, *90*, 97.
(10) Harvey, J. N. *Phys. Chem. Chem. Phys.* **2007**, *9*, 331–343.
(11) (a) Shaik, S.; Filatov, M.; Schroeder, D.; Schwartz, H. *Chem.—Eur. J.* **1998**, *4*, 193–199. (b) Harvey, J. N.; Poli, R.; Smith, K. M. *Coord. Chem. Rev.* **2003**, *238*−*238*, 347–361.
(12) Holm, R. H.; Kennepohl, P.; Solomon, E. I. *Chem. Rev.* **1996**, *96*, 2239–2314.
(13) Chen, P.; Solomon, E. I. *J. Am. Chem. Soc.* **2004**, *126*, 4991–5000.
(14) Klotz, I. M.; Kurtz, D. M., Jr. *Chem. Rev.* **1994**, *94*, 567–568.
(15) Bakac, A. *Coord. Chem. Rev.* **2006**, *250*, 2046–2058.
(16) Lewis, E. A.; Tolman, W. B. *Chem. Rev.* **2004**, *104*, 1047–1076.
(17) Böttcher, A.; Elias, H.; Müller, L.; Paulus, H. *Angew. Chem., Int. Ed.* **1992**, *31*, 623–625.
(18) Hausinger, R. P. *J. Biol. Inorg. Chem.* **1997**, *2*, 279–286.
(19) Smith, M. C.; Barclay, J. E.; Davies, S. C.; Hughes, D. L.; Evans, D. J. *Dalton Trans.* **2003**, 4147–4151.
(20) Kieber-Emmons, M. T.; Riordan, C. G. *Acc. Chem. Res.* **2007**, *40*, 618–625.

(21) Kieber-Emmons, M. T.; Annaraj, J.; Seo, M. S.; Van Heuvelen, K. M.; Tosha, T.; Kitagawa, T.; Brunold, T. C.; Nam, W.; Riordan, C. G. *J. Am. Chem. Soc.* **2006**, *128*, 14230–14231.
(22) Yao, S.; Bill, E.; Milsmann, C.; Wieghardt, K.; Driess, M. A. *Angew. Chem., Int. Ed.* **2008**, *47*, 110–7113.
(23) Fujita, K.; Schenker, R.; Gu, W.; Brunold, T. C.; Cramer, S. P.; Riordan, C. G. *Inorg. Chem.* **2004**, *43*, 3324–3326.
(24) (a) Bogus, W.; Kevan, L. *J. Phys. Chem.* **1989**, *93*, 3223–3226. (b) Azuma, N.; Hartmann, M.; Kevan, L. *J. Phys. Chem.* **1995**, *99*, 6670–6676.
(25) Telser, J. *J. Braz. Chem. Soc.* **2010**, *21*, 1139–1157.
(26) de la Lande, A.; Salahub, D. R.; Maddaluno, J.; Scemana, A.; Pilme, J.; Parisel, O.; Gerard, H.; Caffarel, M.; Piquemal, J.-P. *J. Comput. Chem.* **2011**, *32*, 1178–1182.
(27) van Lenthe, E.; Baerends, E. J.; Snijders, J. G. *J. Chem. Phys.* **1993**, *99*, 4597–4610.
(28) Neese, F. *J. Chem. Phys.* **2001**, *115*, 11080–11096.
(29) Schreckenbach, G.; Ziegler, T. *J. Phys. Chem. A* **1997**, *101*, 3388–3399.
(30) Stadler, C.; de Lacey, A. L.; Hernandez, B.; Fernandez, V. M.; Conesa, J. C. *Inorg. Chem.* **2002**, *41*, 4417–4423.
(31) Craft, J. L.; Mandimutsira, B. S.; Fujita, K.; Riordan, C. G.; Brunold, T. C. *Inorg. Chem.* **2003**, *42*, 859–867.
(32) Ray, K.; Weyhermuller, T.; Neese, F.; Wieghardt, K. *Inorg. Chem.* **2005**, *44*, 5345–5360.
(33) Sojka, Z.; Pietrzyk, P.; Martra, G.; Kermarec, M.; Che, M. *Catal. Today* **2006**, *114*, 154–161.
(34) Pietrzyk, P.; Sojka, Z. *J. Phys. Chem. A* **2005**, *109*, 10571–10581.
(35) Pietrzyk, P.; Podolska, K.; Sojka, Z. *Chem.—Eur. J.* **2009**, *15*, 11802–11807.
(36) Patchkovskii, S.; Ziegler, T. *J. Chem. Phys.* **1999**, *111*, 5730–5740.
(37) Spalek, T.; Pietrzyk, P.; Sojka, Z. *J. Chem. Inf. Model.* **2005**, *45*, 18–29.
(38) Dyrek, K.; Che, M. *Chem. Rev.* **1997**, *97*, 305–331.
(39) te Velde, G.; Bickelhaupt, F. M.; Baerends, E. J.; Fonseca Guerra, C.; van Gisbergen, S. J. A.; Snijders, J. G.; Ziegler, T. *J. Comput. Chem.* **2001**, *22*, 931–967.
(40) *ADF2007.01, SCM, Theoretical Chemistry*; Vrije Universiteit: Amsterdam, The Netherlands (http://www.scm.com).
(41) Becke, A. D. *J. Chem. Phys.* **1988**, *88*, 2547–2553.
(42) Perdew, J. P.; Wang, Y. *Phys. Rev. B* **1992**, *45*, 13244–13249.
(43) (a) Becke, A. D. *Phys. Rev. A* **1988**, *38*, 3098–3100. (b) Perdew, J. P. *Phys. Rev. B* **1986**, *33*, 8822–8824.
(44) Mitoraj, M.; Michalak, A. *J. Mol. Model.* **2007**, *13*, 347–355.
(45) Michalak, A.; Mitoraj, M.; Ziegler, T. *J. Phys. Chem. A* **2008**, *112*, 1933–1939.
(46) van Wüllen, C. *J. Comput. Chem.* **2002**, *23*, 779–785.
(47) Neese, F. *ORCA—An ab initio, Density Functional and Semi-empirical Program Package*, Version 2.6-00; Lehrstuhl für Theoretische Chemie: Bonn, 2007.
(48) Schäfer, A.; Huber, C.; Ahlrichs, R. *J. Chem. Phys.* **1994**, *100*, 5829–5835.
(49) Neese, F. *Inorg. Chim. Acta* **2002**, *337*, 181–192.
(50) Neese, F. *J. Chem. Phys.* **2003**, *118*, 3939–3948.
(51) Barone, V. In *Recent Advances in Density Functional Methods, Part I*; Chong, D. P., Ed.; World Scientific: Singapore, 1996.
(52) Serykh, A. I.; Amiridis, M. D. *J. Phys. Chem. C* **2007**, *111*, 17020–17024.
(53) Pietrzyk, P.; Podolska, K.; Sojka, Z. *J. Phys. Chem. C* **2011**, *115*, 13008–13015.
(54) Che, M.; Tench, A. J. *Adv. Catal.* **1982**, *31*, 77–133.
(55) The decay of the EPR signal of the superoxide is most probably caused by its transformation into the diamagnetic peroxo species by surface disproportionation ($2O_2^- \rightarrow O_2^{2-} + O_2$) as discussed earlier. Che, M.; Sojka, Z. *Top. Catal.* **2001**, *15*, 211–217.
(56) Provisionally acceptable parameters were also obtained for the μ-{Ni(μ-1,2-O_2)Ni}^{19}[$(H_2O)_2(OH)$]$_2$, but subsequent calculations using a robust μ-{Ni(μ-1,2-O_2)Ni}^{19}**M7**−**M5** model that takes into account the zeolite hosting center revealed that this coordination mode can be disregarded.
(57) Cramer, C. J.; Tolman, W. B.; Theopold, K. H.; Rheingold, A. L. *Proc. Natl. Acad. Sci. U.S.A.* **2003**, *100*, 3635–3640.
(58) Yao, S.; Bill, E.; Milsmann, C.; Wieghardt, K.; Driess, M. *Angew. Chem., Int. Ed.* **2008**, *47*, 7110–7113.
(59) Chiesa, M.; Giamello, E.; Paganini, M. C.; Sojka, Z.; Murphy, D. M. *J. Chem. Phys.* **2002**, *116*, 4266–4274.
(60) Bickelhaupt, F. M.; Baerends, E. J. In *Reviews in Computational Chemistry*; Lipkowitz, K. B., Boyd, D. B., Eds.; Wiley-VCH: New York, 2000; Vol. 15, pp 1−86.
(61) Schreckenbach, G.; Ziegler, T. *J. Phys. Chem.* **1995**, *99*, 606–611.
(62) Pietrzyk, P.; Podolska, K.; Sojka, Z. *J. Phys. Chem. A* **2008**, *112*, 12208–12219.
(63) Känzig, W.; Cohen, M. H. *Phys. Rev. Lett.* **1959**, *3*, 509–510.
(64) Weltner, W., Jr. *Magnetic Atoms and Molecules*; Dover Publications, Inc.: New York, 1983; p 346.
(65) Kimura, E.; Machida, R.; Kodama, M. *J. Am. Chem. Soc.* **1984**, *106*, 5497–5505.
(66) Goldcamp, M. J.; Robinson, S. E.; Krause Bauer, J. A.; Baldwin, M. *Inorg. Chem.* **2002**, *41*, 2307–2309.